Geophysical Prospecting

EAGE EUROPEAN ASSOCIATION OF GEOSCIENTISTS & ENGINEERS

Geophysical Prospecting, 2018, **66**, 1111–1122 doi: 10.1111/1365-2478.12634

High-resolution multi-component distributed acoustic sensing

Ivan Lim Chen Ning* and Paul Sava

Center for Wave Phenomena, Colorado School of Mines, 1500 Illinois St., Golden, CO 80401, USA

Received July 2017, revision accepted February 2018

ABSTRACT

Distributed acoustic sensing uses an optical fibre together with an interrogator unit to perform strain measurements. The usage of distributed acoustic sensing in geophysics is attractive due to its dense spatial sampling and low operation cost if the optical fibre is freely accessible. In the borehole environment, optical fibres for distributed acoustic sensing are often readily available as a part of other sensing tools, such as for temperature and pressure. Although the distributed acoustic sensing system promises great potential for reservoir monitoring and surface seismic acquisition, the single axial strain measurement of distributed acoustic sensing along the fibre is inadequate to fully characterise the different wave modes, thus making reservoir characterisation challenging. We propose an acquisition system using five equally spaced helical optical fibres and a straight optical fibre to obtain six different strain projections. This system allows us to reconstruct all components of the 3D strain tensor at any location along the fibre. Analysing the condition number associated with the geometry of the optical fibre, we can systematically search for the optimum design parameters for our configuration. Numerical examples demonstrate the effectiveness of our proposed method to successful reconstruction of the full strain tensor from elastic wavefields of arbitrary complexity.

Key words: Multi-component, Seismic acquisition, Data reconstruction.

INTRODUCTION

Distributed acoustic sensing (DAS) systems use an optical fibre as a distributed array of strain measuring tool. A typical DAS system employs an interrogator unit to send laser pulses into an optical fibre and detect back-scattered light along the fibre. DAS systems that operate on coherent optical time-domain reflectometry (COTDR) provide average axial strain measurement through analysing the perturbed phase difference between back-scattered light along the optical fibre from two points separated by a distance known as gauge length. Acceptable signal-to-noise ratio (SNR) measurements can be achieved using conventional DAS systems that require a gauge length of around 1 m. However, Farhadiroushan, Parker and Shatalin (2016) show that the gauge length can be reduced to 5 cm, while maintaining satisfactory SNR using specially designed optical fibres.

Despite the recent technological advances in DAS, multi-component DAS remains a missing piece of the puzzle to capture the full character of the seismic wavefield. In borehole application specifically, the usage of DAS focuses mainly on reservoir imaging (Mestayer *et al.* 2011; Mateeva *et al.* 2012, 2013; Wu *et al.* 2015; Zhan, Kommedal and Nahm 2015; Jiang *et al.* 2016) and velocity model updates (Li *et al.* 2015; Wu *et al.* 2015). Although, many examples show that DAS has the potential to provide low-cost reservoir monitoring (Hornman *et al.* 2015; Chalenski *et al.* 2016; Dou *et al.* 2016), the conventional single component DAS measurements makes reservoir characterisation challenging. Since DAS acquires strain along the optical fibre, the measurement is a projection of the surrounding strain tensor as a function of the optical fibre position. As indicated by Lumens (2014) and

*E-mail: ivanlimchenning@mines.edu

© 2018 European Association of Geoscientists & Engineers

Bakku (2015), the DAS system suffers from broadside sensitivity where the optical fibre is less sensitive to transversally impinging signals.

Although DAS measures axial strain, it is possible to obtain multi-component data by reconstructing the entire strain tensor using multiple strain projections; manipulating the geometry of the optical fibre allows us to obtain various directions on which to project the strain field. Lim Chen Ning and Sava (2016) provide a basic workflow for recovering multi-component DAS data using strain projections acquired with dual optical fibres or with a single chirping (variable pitch angle) helical optical fibre. The pitch angle is the complement of the angle between the tangent vector and the axial direction of the DAS cable. The dual optical fibres configuration deploys two helical optical fibre of different constant pitch angle. This configuration is necessary to obtain sufficient projections for the strain tensor reconstruction. Similarly, Lim Chen Ning and Sava (2016) demonstrate the possibility of full strain tensor reconstruction using one optical fibre with a chirping helix geometry, which provides a broad range of strain projections, albeit at the expense of a complex design. The underlying principle of their method of strain tensor reconstruction is to group consecutive strain measurements along optical fibre(s) within a defined window larger than a gauge length. Despite successfully reconstructing the entire strain tensor, the drawback of this method is the assumption that the seismic wavelength is significantly larger than the defined analysis window. This assumption leads to a strain tensor that is assumed to be invariant within the window. Therefore, the method proposed by Lim Chen Ning and Sava (2016) could not be easily used for acquisition of short seismic wavelengths such as microseismic.

To overcome the limitation of the workflow introduced by Lim Chen Ning and Sava (2016), we propose a configuration with five equally spaced constant pitch angle helical optical fibre and a straight optical fibre. Although we use an increased number of optical fibres, we can obtain six different strain projections at every location and avoid the need to group consecutive strain measurements at different location along optical fibre(s) to get sufficient strain projections for the reconstruction. We thus obtain six different strain projections at every location and reconstruct the full strain tensor without the need to assume invariance in a wide window. The configuration reduces the engineering complexity required to build a multi-fibre cable, and also allows us to systematically analyse the effect of the associated design parameters (gauge length, diameter and pitch angle of the helical optical fibres) on the strain tensor reconstruction. We capture the gauge length in the reconstruction process, which allows us to remove its averaging effect and reconstruct strain data similar to multi-component geophone point measurements. We note, however, that our method provides the entire strain tensor in contrast to geophone measurements that provide the displacement vector.

We demonstrate a systematic way to choose the helical optical fibre design parameters (diameter and pitch angle) and the gauge length characterising our system by analysing the condition number associated with the geometry our configuration. Using the chosen parameters, we show the reconstruction of the full strain tensor through 3D synthetic examples of arbitrarily complex seismic wavefields.

THEORY

The axial strain acquired by DAS captures different projections of the surrounding strain tensor as a function of the location and geometry of the optical fibre. We use the intrinsic coordinate system of a curve as described by Lin and Pisano (1988) to express the local coordinate system of the optical fibre with respect to a global coordinate system. We use the tangent vector along the optical fibre to relate the axial strain measurement with the surrounding strain tensor. The relationship between the axial strain and the surrounding strain tensor is given through the coordinate transformation relationship (Young and Budynas 2002)

$$\bar{\boldsymbol{\varepsilon}} = \mathbf{R}\boldsymbol{\varepsilon}\mathbf{R}^{\mathrm{T}}, \tag{1}$$

where $\bar{\boldsymbol{\varepsilon}}$ and $\mathbf{R}$ denote the transformed strain tensor and the transformation (also known as rotation) matrix, respectively. As derived in Appendix, we rearrange equation (1) as

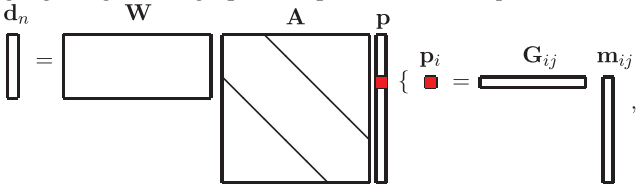
$$\mathbf{p} = \mathbf{G}\mathbf{m}, \tag{2}$$

where $\mathbf{p}$ and $\mathbf{m}$ are the transformed and original strain tensors, respectively in vector form. The matrix $\mathbf{G}$ is the expansion of equation (3) using the transformation matrix $\mathbf{R}$ and contains all the geometric information about the optical fibre. For a single optical fibre, we have infinitely many strain projections along the optical fibre, where every projection being characterised by equation (2). To fully describe the DAS measurements $\mathbf{d}$, we use equation (2) and account for the axial strain averaging effect due to the gauge length as

$$\mathbf{d} = \mathbf{W}\mathbf{A}\mathbf{G}\mathbf{m}, \tag{3}$$

where $\mathbf{A}$ is a convolution operator describing strain averaging within a gauge length, and $\mathbf{W}$ is a windowing operator that defines the channel spacing which refers to the distance

between consecutive average strain measurements within a gauge length. The graphical representation of equation (3) is



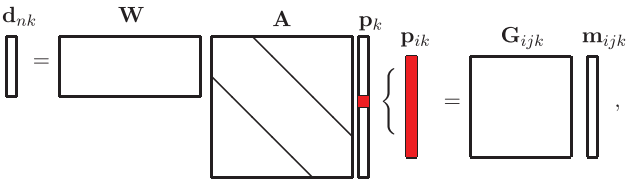
where indices i, j and n represent samples along the optical fibre, components of the strain tensor and measurements of a DAS system, respectively. Every sample i along the optical fibre is an element in the projection vector $\mathbf{p}$. Using the band matrix that describes the convolution operator $\mathbf{A}$, we capture the gauge length effect of the DAS system. In order to replicate a typical DAS system measurement, we apply a windowing operator $\mathbf{W}$ to determine the channel spacing between average strain measurements, usually equal to the gauge length. We represent the cascading operators $\mathbf{WAG}$ as a single linear operator $\mathbf{L}$. If we obtain sufficient strain projections to describe the surrounding strain tensor, we can reconstruct the strain tensor $\mathbf{m}$ in a least-squares sense as

$$\mathbf{m} = (\mathbf{L}^{\mathrm{T}}\mathbf{L})^{-1}\mathbf{L}^{\mathrm{T}}\mathbf{d}. \tag{4}$$

To achieve accurate reconstruction using equation (4), the Gram matrix $\mathbf{L}^{\mathrm{T}}\mathbf{L}$ has to be invertible, that is it has to be full rank, which means that all rows and as columns of the matrix must be linearly independent. The accuracy of the inverse matrix calculation is inferred from its condition number obtained as the ratio of the largest to the smallest singular values. If the condition number is large, then the matrix is ill-conditioned, implying the computation of its inverse tends to be spurious. However, a matrix with low condition number, has an inverse that can be accurately computed. Therefore, it is advantageous to use the condition number as an indicator of strain tensor reconstruction capability. This also provides us with an opportunity to analyse various optical fibre system designs, as discussed later.

Lim Chen Ning and Sava (2016) propose two configurations to obtain multiple strain projections to reconstruct the entire strain tensor. They demonstrate that two helical optical fibres of different constant pitch angles provide sufficient strain projections to accurately reconstruct the entire strain tensor. They also show that a single helical optical fibre with varying pitch angle is capable to provide adequate strain projections to reconstruct the entire strain tensor. In this reconstruction, Lim Chen Ning and Sava (2016) group n consecutive strain measurements (where $n \geqslant 6$ and possibly higher for improved SNR) along the optical fibre(s) within a defined window to obtain $\mathbf{d}$ in equation (4). Similarly, they group the associated linear operators $\mathbf{L}$ to form the Gram matrix. Although they demonstrate successful reconstruction, their approach has the drawback that it assumes a seismic wavelength significantly larger than the defined window for reconstruction. This drawback limits the application of this method to acquisition of long seismic wavelengths, thus reducing the resolution of seismic imaging with DAS data.

To overcome this drawback especially for applications that require short seismic wavelengths, we propose a configuration using six optical fibres to reconstruct all components of the strain tensor. Our approach is similar to the method of Lim Chen Ning and Sava (2016), as we use multiple strain projections to reconstruct the entire strain tensor using the formulation in equation (4). However, our configuration forms a full rank Gram matrix using measurements from individual optical fibres instead of spatially grouping consecutive measurements along a single optical fibre. Our new method allows us to reconstruct the strain tensor $\mathbf{m}$ in equation (4) at any given location using data $\mathbf{d}$ from individual measurements in the constituent optical fibres. The equivalent graphical representation of equation (3) for our proposed method



where index k denotes the number of optical fibre used for projections. Every sample i along the optical fibre k is given as an element in the projection vector $\mathbf{p}_k$. The presences of k optical fibres allow us to form the data vector $\mathbf{d}_{nk}$ and reconstruct the strain tensor $\mathbf{m}$ at a given location n. Note that the minimum requirement is to have $k = 6$ to reconstruct the six components of the strain tensor, which is similar to requirement of the method of Lim Chen Ning and Sava (2016) where they group $n \geqslant 6$ consecutive strain measurements.

We represent individual optical fibres in our proposed configuration with tangent vectors to conceptually visualise the associated measurements as shown in Fig. 1a with different pitch angles from 20° to 70° at every 10°. Fig. 1c demonstrates that by using the same origin for all the vectors, we obtain a right pentagonal pyramid. The geometrical implication of our configuration provides insights on the associated strain projection, as discussed later. Using the projection matrix $\mathbf{G}$ of the individual vectors, we evaluate the singular values of $\mathbf{L}^{\mathrm{T}}\mathbf{L}$ as shown in Fig. 1e, which indicates that our configuration is full rank, despite the fact that the

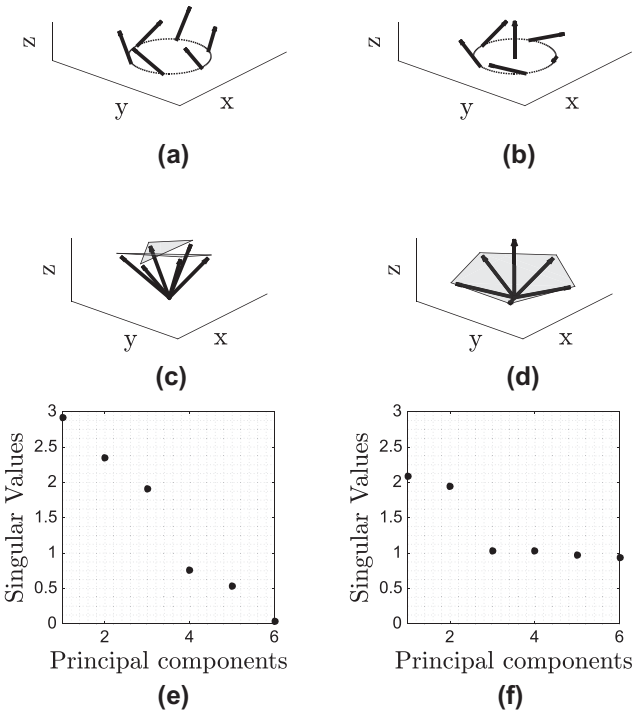


Figure 1 Optical fibre geometry with (a) six equally spaced vectors of six pitch angles (20°, 30°, 40°, 50°, 60° and 70°), and (b) five equally spaced vectors of pitch angle of 20° with a straight vector in the middle. Panels (c) and (d) depict tetrahedra and right pentagonal pyramid, respectively, using the corresponding vectors in (a) and (b) sharing the same origin. The plots in (e) and (f) show singular values of the respective Gram matrices.

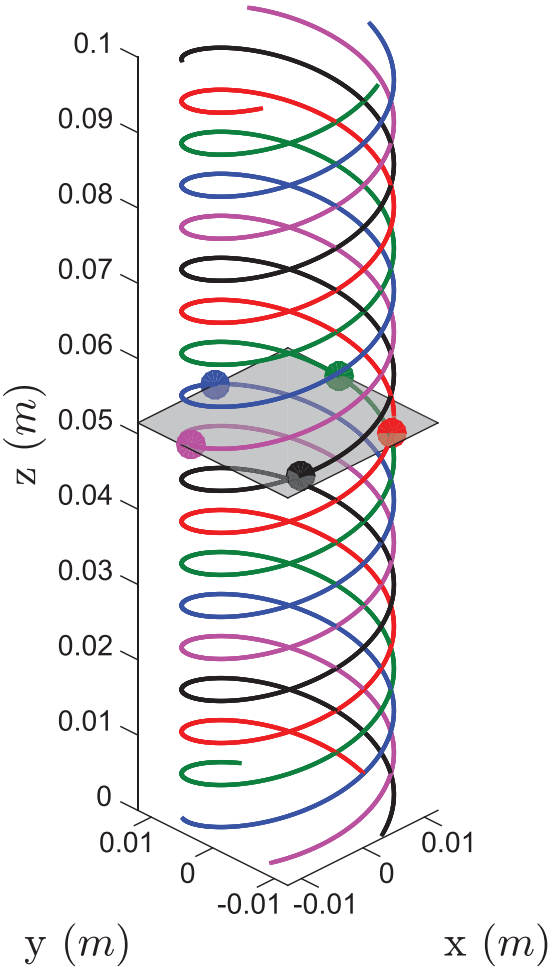


Figure 2 Example of five equally spaced helical optical fibres with a diameter of 2.44 cm and a pitch angle of 20°. The dots represent measurement at the same length along respective fibres, which refer to the same portion of the cable indicated by the horizontal plane. The straight vertical optical fibre is not included in this plot.

smallest singular value is close to zero. A full rank Gram matrix indicates that the corresponding configuration can reconstruct the entire strain tensor. However, using multiple helical optical fibres of different pitch angles increases the engineering complexity required to assemble the optical fibre system.

In order to simplify the design, we set our configuration to five equally spaced helical optical fibre with a 20° pitch angle, together with a straight optical fibre as shown in Fig. 1b. Rearranging the vectors to share the same origin allows us to form a right pentagonal pyramid, as shown in Fig. 1d. The straight fibre makes it possible to have all nonzero singular values, as seen in Fig. 1f, that imply a full rank Gram matrix. This configuration uses five equally spaced helical optical fibres with constant pitch angle that is less manufacturing challenging than a sweeping helical optical fibre and allows us to obtain measurements at the same position in space along all the helical optical fibres (illustrated in Fig. 2).

Using the configuration in Fig. 1b and analysing the condition number of the corresponding Gram matrix, we search for the optimum pitch angle between 5° and 50° as shown (solid line) in Fig. 3. The lowest condition number is around 20°; at this angle, the strain projections are mainly contributed by the horizontal components. The vertical vector in our arrangement provides only vertical strain projections. This implies that to accurately reconstruct the entire strain tensor, lower pitch angles are desirable to obtain projections from horizontal strain components as seen in Fig. 3, where the condition number of the corresponding Gram matrix increases with the pitch angle from 20°. However, we avoid low pitch angles that are near horizontal to obtain projections from

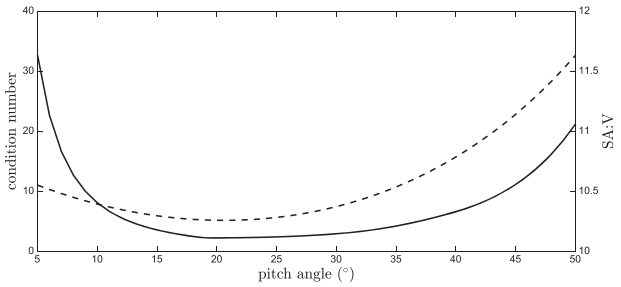


Figure 3 The solid line represents the condition number and the dashed line denotes the surface area to volume ratio (SA:V) of a right pentagonal pyramid at different pitch angles for the five vectors in Fig. 1d. Both graphs share the same minimum at around 20° pitch angle.

strain components between horizontal and vertical (i.e. ε_{xz} and ε_{yz}) for accurate reconstruction of the strain tensor as shown in Fig. 3, where the condition number decreases as the pitch angle approaches 20°.

We investigate the effects of the geometrical change in Fig. 1d associated with the pitch angle of our configuration in Fig. 1b on the condition number of the corresponding Gram matrix. To quantitatively assess the geometrical implication of our configuration in Fig. 1d, which corresponds to a right pentagonal pyramid, we can calculate the surface area to volume ratio (SA:V) as shown (dashed line) in Fig. 3. SA:V provides us a measure of compactness of the geometry associated with our configuration. Fig. 3 shows that the lowest SA:V (most compact geometry) corresponds to the pitch angle around 20°, which coincides with the lowest condition number of the Gram matrix associated with our configuration in Fig. 1b. Observing the geometry for high SA:V at 5° (Fig. 4a) and 50° (Fig. 4c), we can infer that the geometries that are flat or elongated do not provide a low condition numbers and thus do not lead to robust strain reconstruction. However, Fig. 4b reveals a compact geometry with low SA:V that can provide sufficient projections to describe the surrounding strain tensor for full and accurate reconstruction.

We investigate the effects of the gauge length on the Gram matrix by considering single measurements as shown (dots) in Fig. 2. The azimuthal variation of the five equally spaced optical fibres does not affect the Gram matrix as the spacing between measurements is invariant as a function of position along the optical fibre. Using the condition number of the Gram matrix, we can systematically obtain the optimum design parameters (gauge length, diameter and pitch angle of the helical optical fibres) associated with low condition numbers as shown in Fig. 5 (the colours represent the logarithm of condition number). We can scan pitch angles from 15° to 35° and diameters of the helical optical cable from 0.01 to 0.03 m, for specific gauge lengths of 0.2, 0.4, 0.6, 0.8 and 1.0 m.

The strain measurement by the DAS system using a helical geometry undergoes strain averaging in the azimuthal direction along the optical fibre within a gauge length. When the gauge length is equal to a multiple of the helix lead (the axial advance of a helix for a complete 360° turn), the DAS measurement does not contain azimuthal information, which translates into an undeniable high condition number in Fig. 5. If we increase the gauge length for the same diameter and pitch angle (fixed helical optical fibre design parameters), the condition number is increasingly oscillatory, as shown in Fig. 5. The DAS measurement undergoes further azimuthal averaging within a longer gauge length, thus reducing the ability to accurately reconstruct the entire strain tensor. As we decrease the diameter of the helical optical fibres, the oscillations increase in frequency, which is also a result of increased azimuthal averaging. An informed reduction of the design parameters using the condition number ensures a high reconstruction accuracy.

In cases such as a borehole where dimensions (e.g. the diameter) are often limited, we can perform a 2D parameter scan with one of the parameters fixed. In this paper, we show numerical examples of reconstructing the strain tensor using our new approach for identifying optimum parameters for a borehole environment, and we set the diameter of the optical fibre system at 2.44 cm (about 1 inch).

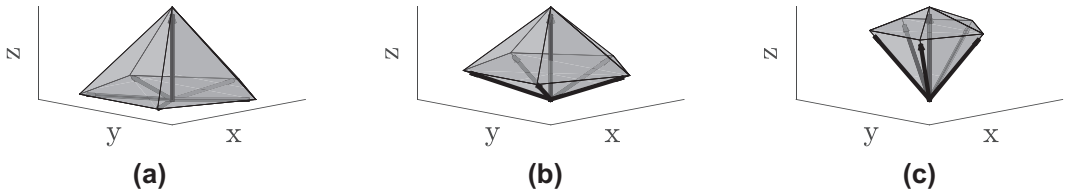


Figure 4 Two pentagonal pyramids using five vectors with pitch angles of (a) 5°, (b) 20° and (c) 50°. The three pyramids show the visual relationship between the enclosed surface area and volume.

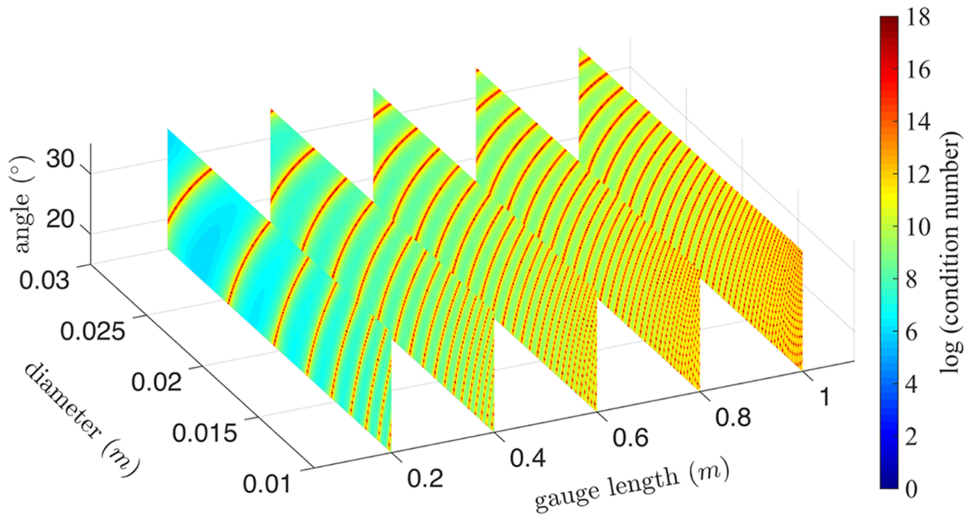


Figure 5 Condition number of the Gram matrix for pitch angle from 15° to 35° and diameter from 0.01 to 0.03 m. These slices are specifically scanned for, but not limited to gauge lengths of 0.2, 0.4, 0.6, 0.8 and 1.0 m.

NUMERICAL EXAMPLES

Using numerical simulations, we reconstruct the entire 3D strain tensor with the parametrisation analysis in a borehole scenario. In the following examples, we limit the dimensions of the helical optical fibres to a diameter of 2.44 cm and a pitch angle of 20° as shown in Fig. 2. By constraining the design parameters for the helical optical fibres, we can search for an optimum gauge length using the condition number of the Gram matrix as shown in Fig. 6a. In our example, we scan between 0.05 and 1.10 m; we observe that there are several local minima corresponding to low condition number throughout Fig. 6a. The corresponding gauge lengths at these local minima are optimal (i.e. higher accuracy) for strain tensor reconstruction. The oscillating characteristic of the condition number in Fig. 6a shows that the gauge length has to be reduced systematically to ensure a low condition number for high reconstruction accuracy. We illustrate our following examples with gauge lengths of 0.1, 0.5 and 1.0 m, as shown (stars) in Fig. 6a. We choose the gauge length of 0.5 m that does not lie at a local minimum to demonstrate that the strain tensor reconstruct of a smaller gauge length may not necessary be superior to a larger gauge length. This phenomenon is shown through a similar level of reconstruction accuracy in Figs 9c (gauge length of 0.5 m) and e (gauge length of 1.0 m). If dimension is not a constraint, we can perform similar parameter scan for a range of diameter by limiting the pitch angle and gauge length as shown in Fig. 6b for diameter between 0.01 and 0.03 m using 20° pitch angle and gauge length of 0.1 m.

Using synthetic examples of a complex wavefield, we illustrate the reconstruction of the 3D strain tensor from axial strain measurements along the proposed optical fibre geometry using different gauge lengths. We simulate using elastic finite-difference modelling a complex wavefield with triplications (Fig. 7d) caused by a velocity model containing a low-velocity Gaussian anomaly, as shown in Fig. 7c. We use smaller than usual gauge lengths such as 0.1 and 0.5 m, which are possible using specially designed optical fibres, as indicated by Farhadiroushan *et al.* (2016). However, we also perform the analysis using a gauge length of 1.0 m to show the effect of a more conventional fibre system.

Our experiment setup with a source indicated by a dot and receivers indicated by a straight line of coordinates (x_b, y_b) is shown in Fig. 7a. Fig. 7b, shown in a strain tensor matrix layout, represents our target strain tensor reconstruction observed along the receiver location at (x_b, y_b). The horizontal and vertical axes of the individual panels represent the reconstructed measurements along the optical fibre and time, respectively. Using a gauge length of 0.1 m, we can reconstruct the strain tensor as shown in Fig. 8a. The difference plot between the observed and reconstructed strain tensor amplified 10 times is shown in Fig. 8b. We measure reconstruction quality with the residual sum of squares normalised as

$$\eta = \frac{\|\mathbf{m}^{obs} - \mathbf{m}^{rec}\|^2}{\|\mathbf{m}^{obs}\|^2} 100, \tag{5}$$

where $\mathbf{m}^{obs}$ represents the observed strain tensor and $\mathbf{m}^{rec}$ represents the reconstructed strain tensor. The scalar values for η using a gauge length of 0.1 m are less than 10^{-4}%. Fig. 8c

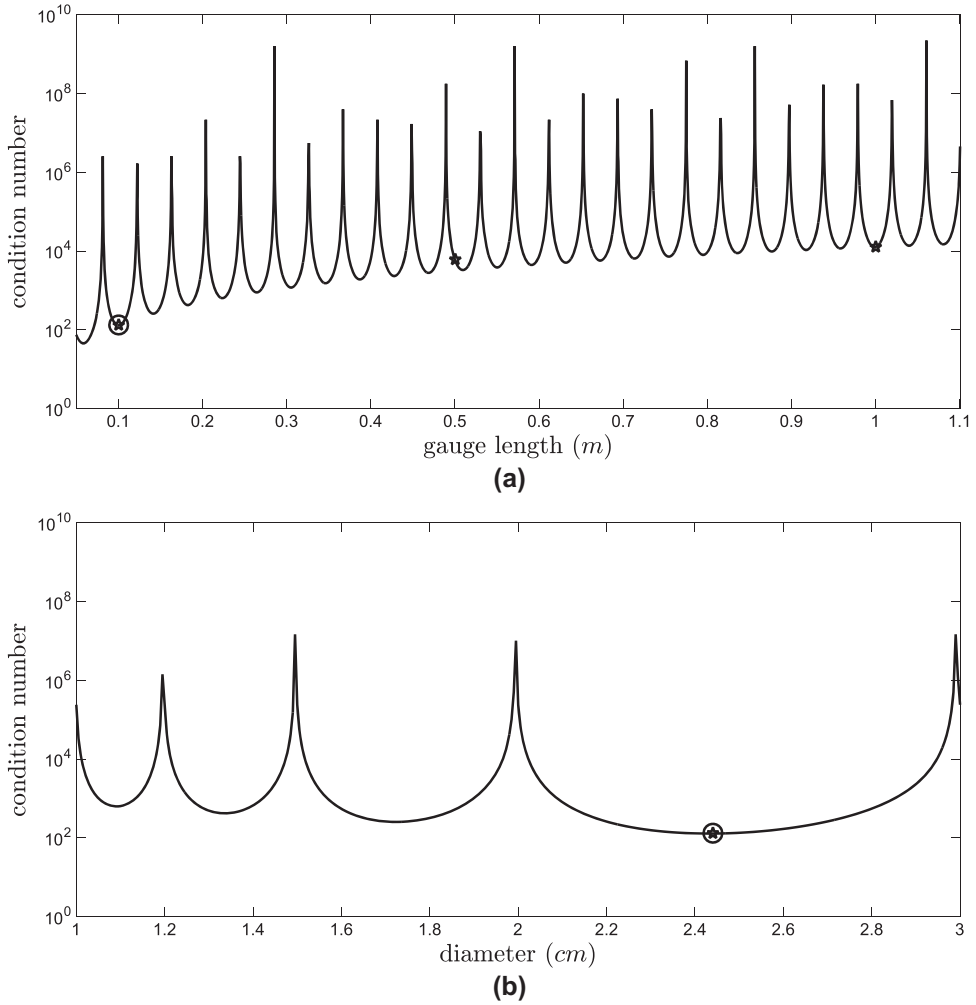


Figure 6 (a) The plot shows a 1D parameter scan for the intersection between diameter of 2.44 cm and 20° pitch angle of Fig. 5. The stars mark the condition number for gauge lengths of 0.1, 0.5 and 1.0 m. (b) The plot shows diameter parameter scan by the fixing pitch angle at 20° and the gauge length at 0.1 m. The star marks the location at diameter of 2.44 cm. The star with circle indicates the same combinations of parameters for both panels.

shows the reconstructed strain tensor using the same configuration, but with the gauge length at 0.5 m. The differences in Fig. 8d (also amplified 10 times) suggest that the increase of gauge length has minimal impact on our reconstruction. Although the calculated values for η increase overall with the larger gauge length, the highest η is less than 10^{-2}%, which is still a very high level of accuracy for practical applications. Fig. 8e shows the results of performing the same reconstruction using a gauge length of 1.0 m. Although we can observe some minor differences in Fig. 8f (also amplified 10 times), the highest η is less than 10^{-2}%, which is lower than the accuracy we get when we use a gauge length of 0.5 m. This result indicates that reducing the gauge length does not necessary improve the reconstruction accuracy; it moreover shows that careful analysis (as presented in Fig. 6a) of the optical fibre parameters is needed for accurate reconstruction. It is worth noting that the parameter combination using gauge length of 0.5 m is not optimal as it does not reside at a local minimum. Such combination of parameters leads to less robust reconstruction under the presence of noise, as shown in Fig. 9c. Diverging further from the local minimum, that is shifting the point for gauge length of 0.5 m as in Fig. 6a to the upward left, increases the noise level in the reconstructed strain tensor tremendously.

Since the strain tensor reconstruction for the gauge lengths of 0.1, 0.5 and 1.0 m is successful without noise, we repeat the process by adding random noise with amplitude up to 30% of the data maximum amplitude (i.e. strain

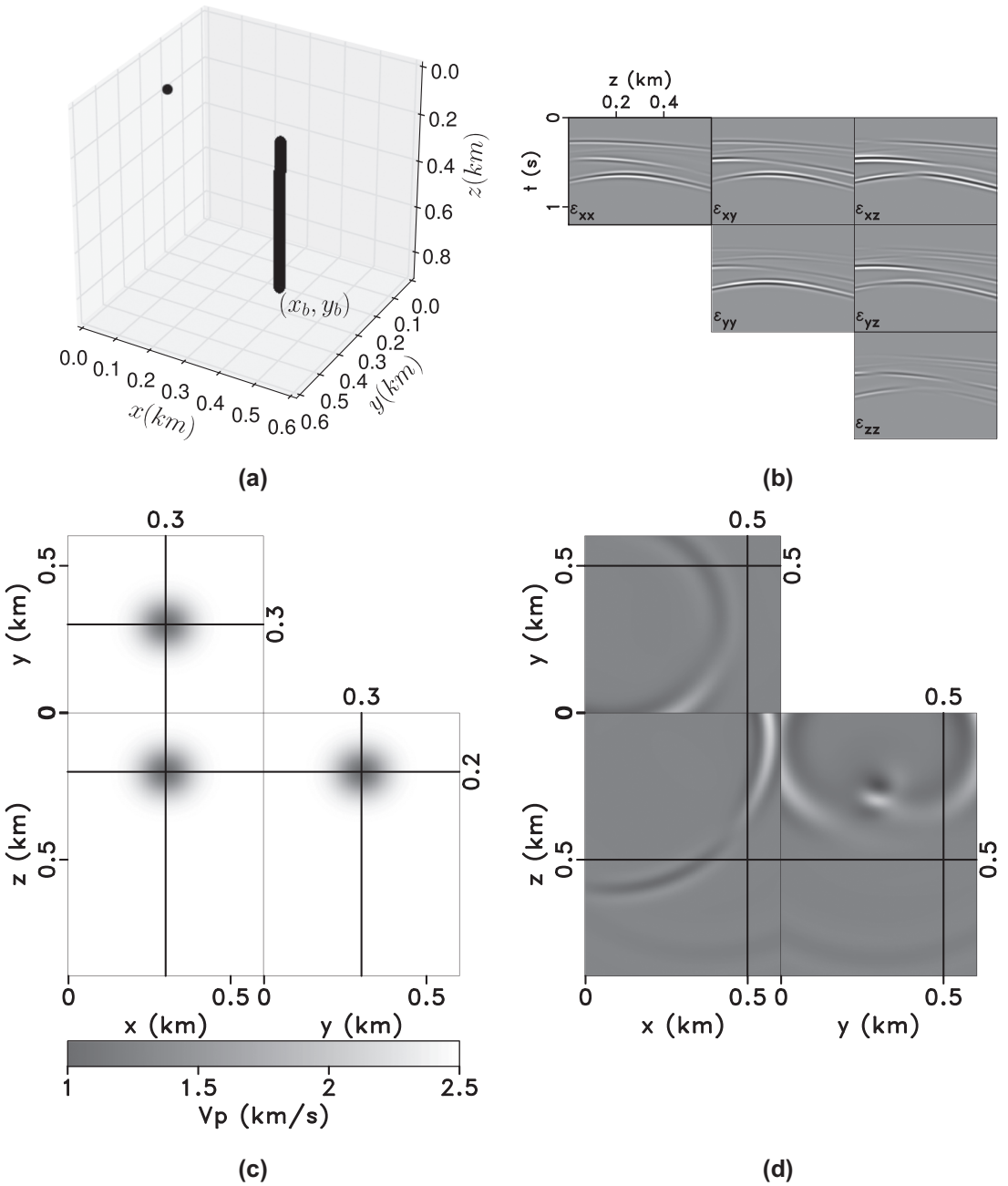


Figure 7 (a) Schematic representation of a DAS experiment depicting the source (dot) and receiver (line) locations. (b) The ideal strain tensor that we would like to reconstruct from DAS measurements. (c) The P-wave velocity model containing a low velocity Gaussian anomaly designed to produce wavefield triplications. The S-wave velocity is half of the P-wave velocity. (d) A snapshot of the vertical displacement wavefield.

projections) and in the data frequency band. In places where the signals are weak, the noise overwhelms the signal. Using a gauge length of 0.1 m, the reconstruction shown in Fig. 9a is a success. The difference plot in Fig. 9b shows primarily random noise. Fig. 9c shows the reconstruction results by increasing the gauge length to 0.5 m. We observe stronger arrivals although the results are noisy. The difference plot shown in Fig. 9d contains primarily noise. Fig. 9e shows the reconstruction using a gauge length of 1.0 m, and it shows a similar result compared to the gauge length of 0.5 m. The same observation applies to the difference plot in Fig. 9f. The comparable quality of reconstruction between gauge length

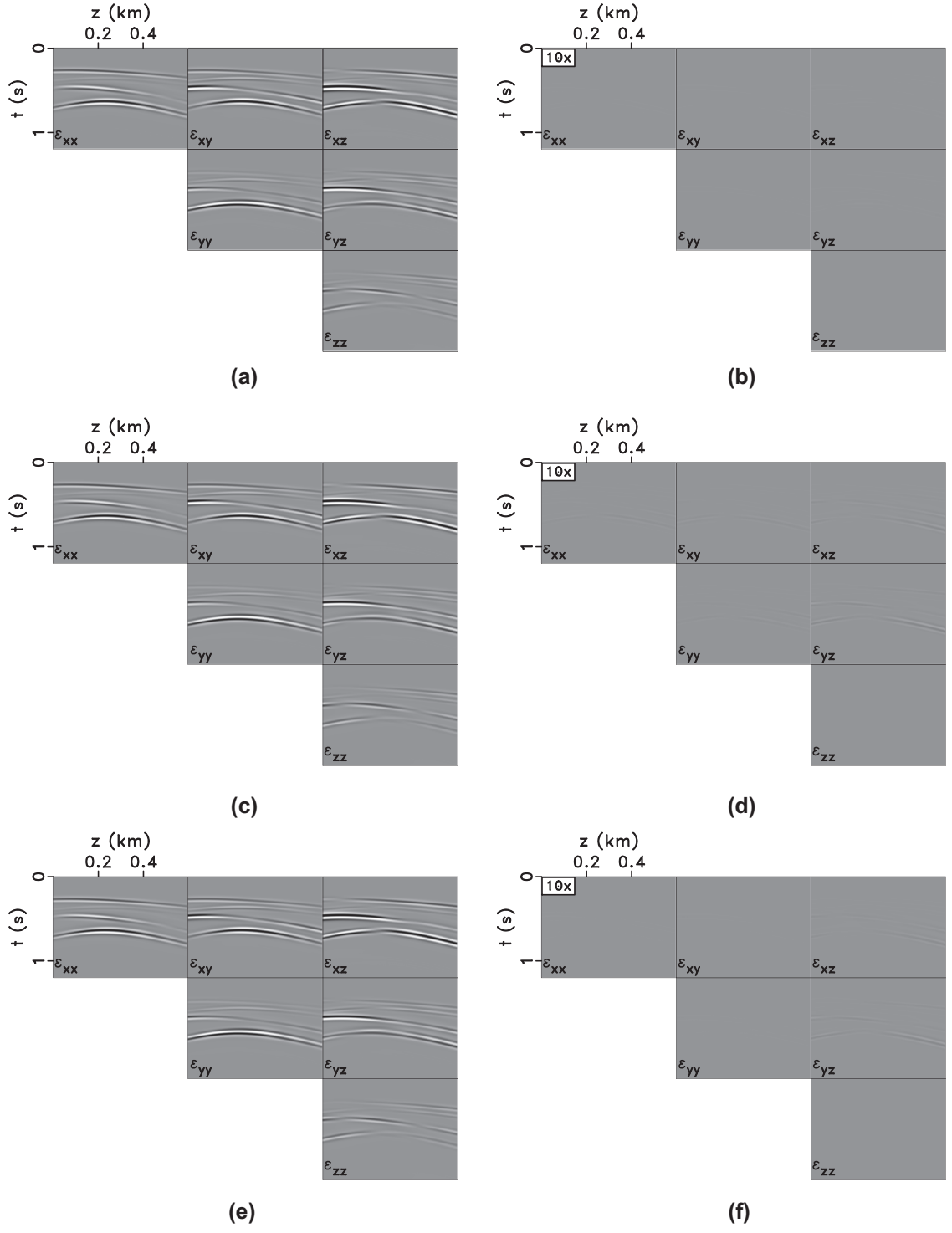


Figure 8 Strain tensor reconstructed with five equally spaced helical optical fibres and a straight optical fibre using a gauge length of (a) 0.1 m, (c) 0.5 m and (e) 1.0 m. (b), (d) and (f) are the difference between the ideal strain tensor in Fig. 7b and the respective reconstructed tensor in (a), (c) and (e) magnified 10 times.

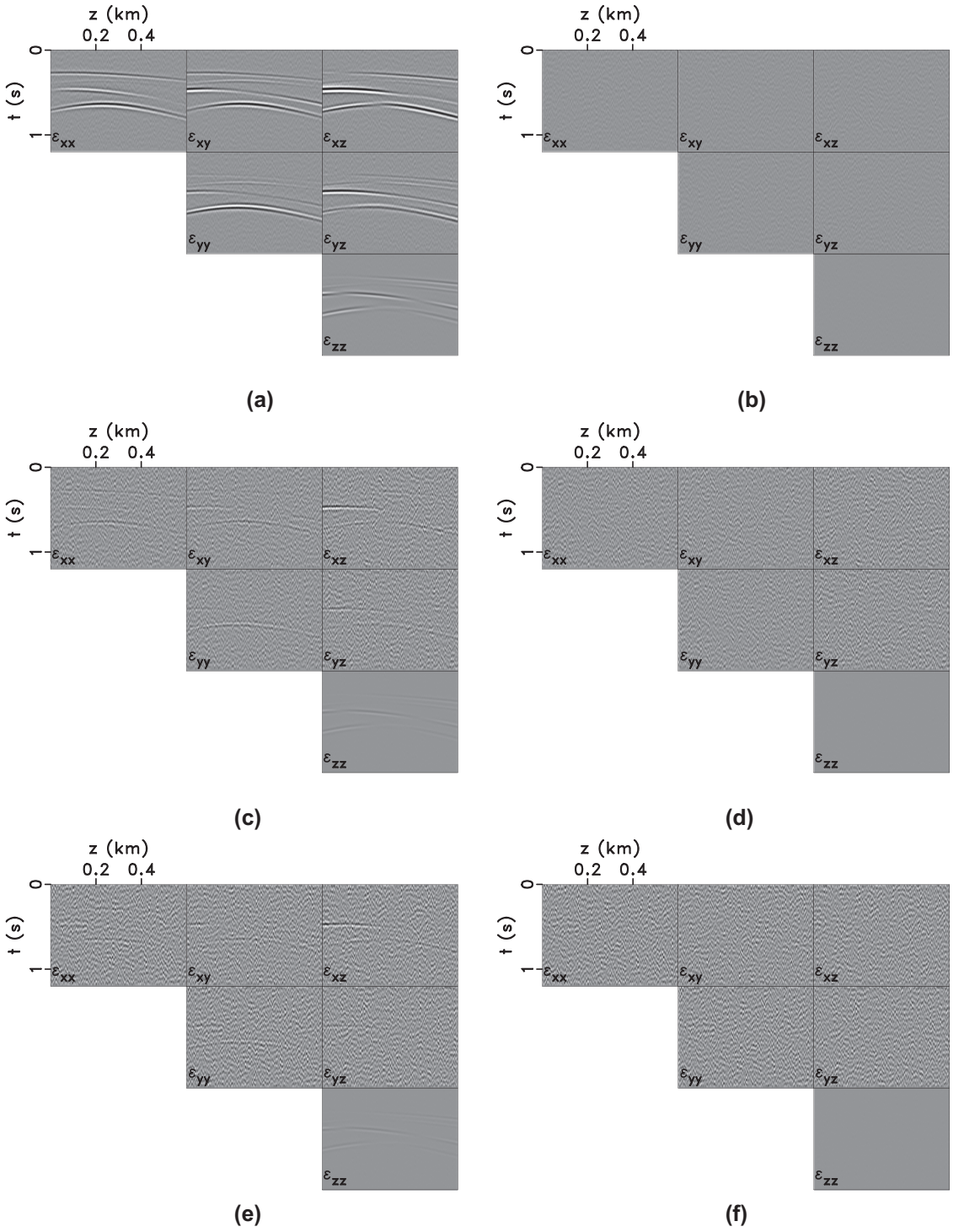


Figure 9 Strain tensor reconstructed from data containing random noise with 30% of the maximum data amplitude and band-limited to the data band with five equally spaced helical optical fibres and a straight optical fibre using a gauge length of (a) 0.1 m, (c) 0.5 m and (e) 1.0 m. (b), (d) and (f) are the difference between the ideal strain tensor in Fig. 7b and the respective reconstructed tensor in (a), (c) and (e).

of 0.5 and 1.0 m shows that reducing gauge length significantly (half in this case) does not necessarily lead to improved reconstruction quality.

DISCUSSION

We demonstrate full strain tensor reconstruction with a high level of accuracy using six optical fibres (five equally spaced helical optical fibre with a pitch angle of 20° and a straight optical fibre). Our results under the presence of noise show the importance of design parameters using the condition number, as reducing the gauge length does not guarantee improvements in reconstruction. However, small but achievable gauge length with low condition number such as 0.1 m provides a robust strain tensor reconstruction due to the low condition number of the Gram matrix. A larger diameter of the helical configuration allows for a larger gauge length that improves the reconstruction results in noisier environments. A relaxed diameter dimension would be more desirable in applications such as in a surface seismic acquisition.

Using our proposed configuration, we can analyse the design parameters for the helical optical fibres systematically. Scanning can be done in a general manner as shown in Fig. 5 or under certain constraints (diameter or pitch angle of the helical optical fibre) as shown in Fig. 6a. The design goal is to obtain parameters that have the lowest possible condition number of the Gram matrix $\mathbf{G}^{\mathrm{T}}\mathbf{A}^{\mathrm{T}}\mathbf{A}\mathbf{G}$ calculated from the averaging $\mathbf{A}$ and projection $\mathbf{G}$ matrices, while also satisfying engineering constraints for optical fibre construction. Numerous configuration of equivalent robustness and quality are possible. In the presence of optical fibre geometry uncertainty, we can use a weighting operator in the reconstruction process or the shape-sensing method (Moore and Rogge 2012), as discussed in our previous paper (Lim Chen Ning and Sava 2016) to improve our reconstruction results.

CONCLUSIONS

We demonstrate that high-resolution multi-component DAS data are achievable by using strain projections along several optical fibres to reconstruct all components of the 3D strain tensor. Five equally spaced helical optical fibres, together with a straight optical fibre can be used for reconstruction without assuming that strain changes slowly along the fibre, as shown by Lim Chen Ning and Sava (2016). We thus overcome the requirement that the seismic wavelength be significantly larger than the window, and achieve multi-component strain reconstruction with high spatial resolution. This method opens the possibility for acquisition of shorter seismic wavelengths, which aids imaging and reservoir characterisation applications. Numerical examples show that our method can reconstruct the full 3D strain tensor for wavefields of arbitrary complexity, and in the presence of strong noise in the band of the seismic data.

ACKNOWLEDGEMENTS

We would like to thank the sponsors of the Center for Wave Phenomena, whose support made this research possible and Martin Karrenbach of OptaSense for fruitful discussions. The reproducible numeric examples in this paper use the Madagascar open-source software package (Fomel *et al.* 2013) freely available from http://www.ahay.org.

ORCID

Ivan Lim Chen Ning
http://orcid.org/0000-0003-3839-9101

REFERENCES

Bakku S.K. 2015. *Fracture characterization from seismic measurements in a borehole*. PhD thesis, Massachusetts Institute of Technology, Cambridge, MA.

Chalenski D., Tatanova M., Du Y., Mateeva A., Lopez J. and Potters H. 2016. Climbing the staircase of ultralow-cost 4D monitoring of deepwater fields using DAS-VSP. 86th Annual International Meeting, SEG, Expanded Abstracts, 5441–5445.

Dou S., Ajo-Franklin J., Daley T., Robertson M., Wood T., Freifeld B. *et al.* 2016. Surface orbital vibrator (SOV) and fiber-optic DAS: field demonstration of economical, continuous-land seismic time-lapse monitoring from the Australian CO2CRC Otway site. 86th Annual International Meeting, SEG, Expanded Abstracts, 5552–5556.

Farhadiroushan M., Parker T. and Shatalin S. 2016. Method and apparatus for optical sensing. WO Patent App. PCT/GB2016/050, 625.

Fomel S., Sava P., Vlad I., Liu Y. and Bashkardin V. 2013. Madagascar: open-source software project for multidimensional data analysis and reproducible computational experiments. *Journal of Open Research Software* **1**, e8.

Hornman J., Mateeva A., Potters J. and Lopez J. 2015. New concepts for lowering the cost of frequent seismic reservoir monitoring onshore. 85th Annual International Meeting, SEG, Expanded Abstracts, 5518–5522.

Jiang T., Zhan G., Hance T., Sugianto S., Soulas S. and Kjos E. 2016. Valhall dual-well 3D DAS VSP field trial and imaging for active wells. 86th Annual International Meeting, SEG, Expanded Abstracts, 5582–5586.

Li Y., Wu H., Wong W., Hewett B., Liu Z., Mateeva A. *et al.* 2015. Velocity analysis and update with 3D DAS-VSP to improve

borehole/surface seismic images. 85th Annual International Meeting, SEG, Expanded Abstracts, 5285–5289.

Lim Chen Ning I. and Sava P. 2016. Multicomponent distributed acoustic sensing. 86th Annual International Meeting, SEG, Expanded Abstracts, 5597–5602.

Lin Y. and Pisano A.P. 1988. The differential geometry of the general helix as applied to mechanical springs. *Journal of Applied Mechanics* **55**, 831–836.

Lumens P.G.E. 2014. *Fibre-optic sensing for application in oil and gas wells*. PhD thesis, Technische Universiteit Eindhoven, The Netherlands.

Mateeva A., Lopez J., Mestayer J., Wills P., Cox B., Kiyashchenko D. *et al.* 2013. Distributed acoustic sensing for reservoir monitoring with VSP. *The Leading Edge* **32**, 1278–1283.

Mateeva A., Mestayer J., Cox B., Kiyashchenko D., Wills P., Lopez J. *et al.* 2012. Advances in distributed acoustic sensing (DAS) for VSP. 82nd Annual International Meeting, SEG, Expanded Abstracts, 1–5.

Mestayer J., Cox B., Wills P., Kiyashchenko D., Lopez J., Costello M. *et al.* 2011. Field trials of distributed acoustic sensing for geophysical monitoring. 81st Annual International Meeting, SEG, Expanded Abstracts, 4253–4257.

Moore J.P. and Rogge M.D. 2012. Shape sensing using multi-core fiber optic cable and parametric curve solutions. *Optics Express* **20**, 2967–2973.

Wu H., Wong W.F., Yang Z., Wills P., Lopez J., Li Y. *et al.* 2015. Dual-well 3D vertical seismic profile enabled by distributed acoustic sensing in deepwater Gulf of Mexico. *Interpretation* **3**, SW11–SW25.

Young W.C. and Budynas R.G. 2002. *Roark's Formulas for Stress and Strain*, Vol. 7. New York: McGraw-Hill.

Zhan G., Kommedal J. and Nahm J. 2015. VSP field trials of distributed acoustic sensing in Trinidad and Gulf of Mexico. 85th Annual International Meeting, SEG, Expanded Abstracts, 5539–5543.

APPENDIX

The strain projection measurement of the surrounding strain tensor along the optical fibre can be expressed through coordinate transformation as (Young and Budynas 2002)

$$\bar{\boldsymbol{\varepsilon}} = \mathbf{R}\boldsymbol{\varepsilon}\mathbf{R}^{\mathrm{T}}, \tag{A1}$$

where $\bar{\boldsymbol{\varepsilon}}$ and $\boldsymbol{\varepsilon}$ denote the strain tensors in the new and original coordinate systems, respectively. **R** represents the transformation (also known as rotation) matrix. Since the transformation matrix is given by the directional cosines between the intrinsic and global coordinate system, the transformation matrix can be expressed through the intrinsic coordinate system using tangent, **t**; normal, **n** and binormal, **b**, unit vectors with respect to the global coordinate system as

$$\mathbf{R} = \begin{bmatrix} R_{11} & R_{12} & R_{13} \\ R_{21} & R_{22} & R_{23} \\ R_{31} & R_{32} & R_{33} \end{bmatrix} = \begin{bmatrix} t_x & t_y & t_z \\ n_x & n_y & n_z \\ b_z & b_y & b_z \end{bmatrix}, \tag{A2}$$

where the rows of the transformation matrix **R** is represented by the tangent, $\mathbf{t} = \{t_x, t_y, t_z\}$; normal, $\mathbf{n} = \{n_x, n_y, n_z\}$ and binormal, $\mathbf{b} = \{b_x, b_y, b_z\}$ unit vectors of intrinsic coordinate system. Since DAS measures axial strain along the optical fibre, it is sufficient to use the tangent vector, **t**, of the optical fibre to perform the axial strain tensor projection. Hence, we can narrow equation (A1) to the rotated axial strain measurement in 3D at a location along the optical fibre as follows:

$$\underset{\mathbf{p}}{\begin{bmatrix} \bar{\varepsilon}_t \end{bmatrix}} = \underset{\mathbf{G}}{\begin{bmatrix} R_{11}^2 & R_{12}^2 & R_{13}^2 & 2R_{11}R_{12} & 2R_{11}R_{13} & 2R_{12}R_{13} \end{bmatrix}} \underset{\mathbf{m}}{\begin{bmatrix} \varepsilon_{xx} \\ \varepsilon_{yy} \\ \varepsilon_{zz} \\ \varepsilon_{xy} \\ \varepsilon_{xz} \\ \varepsilon_{yz} \end{bmatrix}}, \tag{A3}$$

where the projected strain data, **p**, represents strain projection measurements $\bar{\varepsilon}_t$ onto the tangent vector, **t**. The matrix **G** represents the expanded rotation matrix from equation (A2). **m** is the vectorised strain tensor $\boldsymbol{\varepsilon} = \{\varepsilon_{xx}, \varepsilon_{yy}, \varepsilon_{zz}, \varepsilon_{xy}, \varepsilon_{xz}, \varepsilon_{yz}\}$ on the original coordinate system.